Unveiling the deformation mechanism of highly deformable magnesium alloy with heterogeneous grains

Zhi Zhang [a], Jinghuai Zhang [a,*], Wenke Wang [b], Shujuan Liu [c], Bin Sun [a], Jinshu Xie [a], Tingxu xiao [a]

[a] Key Laboratory of Superlight Material and Surface Technology, Ministry of Education, College of Materials Science and Chemical Engineering, Harbin Engineering University, Harbin 150001, China
[b] School of Materials Science and Engineering, Harbin Institute of Technology, Weihai 264209, China
[c] Department of Materials Physics and Chemistry, Harbin Institute of Technology, Harbin 150001, China

ARTICLE INFO

ABSTRACT

Poor formability at room temperature is a key problem that limits the application of Mg alloys. Formability is closely dependent on both large work-hardening capacity and high tensile elongation. Herein, we develop a Mg-3Al-1Zn-0.4Mn (wt%) alloy with heterogeneous grains, obtaining an exceptionally high difference between ultimate tensile strength (UTS) and yield strength (YS) (UTS−YS: 164 MPa) and a good tensile elongation (22%). The uneven deformation of large and small grains is mainly affected by the size difference between grains rather than texture. The high strain hardening is attributed to the pile-up of geometrically necessary dislocations at grain boundaries between large and small grains due to uneven microstrain. The fraction of non-basal dislocations increases greatly with the increase of tensile strain, contributing to the improved ductility. Thus, we put forward a new strategy for improving the formability potential of Mg alloys via introducing heterogeneous-grained structure.

Magnesium (Mg) alloys, the lightest metal structural materials (pure Mg density: ~1.74 g/cm^3), possess high specific strength and good damping capacity, offering a considerable application potential for aerospace, military hardware, automotive, 3C (computer, communication, and consumer electronic) and other fields [1–4]. Nevertheless, Mg alloys also have inherent disadvantages, such as poor formability at room temperature (RT), resulting in insufficiency for the forming of many structural components [3–5].

Numerous efforts and attempts have been made in the past few years to overcome this bottleneck of Mg alloys [6–10]. Basal texture weakening/randomization via alloying and process control, expressed by basal pole figures, is the common method to study and improve the formability of Mg alloys [4,6–9]. It has been reported that elements such as rare earth (RE) and Ca could randomize/weaken the basal texture of Mg alloys. Kim et al. [4] designed a novel Mg-3Al-1Zn-1Mn-0.5Ca (wt%) alloy with a weak texture consisting of split basal poles along rolling direction caused by Ca/Zn grain boundary (GB) co-segregation, obtaining a high formability at RT. Huang et al. [6–8] and Bian et al. [9] proposed the new processes such as high-temperature final rolling

for weakening basal texture in Mg-Al based alloys. In addition, there are a few reports that alloying elements promote the formability of Mg alloys by forming deformable precipitates such as Al$_2$Ca [8,10]. On the whole, the mechanism explanation of formability (plastic deformation) is somewhat inadequate, such as rare observation of in-situ microstructure evolution, and thus the detailed internal mechanism still needs to be further studied.

High formability is strongly correlated to both high tensile elongation and large work-hardening capacity [10,11]. Kim et al. [11] studied detailedly the relationship between formability and uniform elongation/work-hardening capacity of Mg alloys at RT, and reported that the high formability is more closely related with large work-hardening capacity in case of high uniform elongation, rather than yield strength (YS) or uniform elongation alone, regardless of alloy composition. A typical example is that Zhu et al. [10] predicted the high formability of Mg-6Al-1Ca (wt%) alloy by taking advantage of the high elongation (27%) and large work-hardening capacity, in which the work-hardening capacity was evaluated by the difference value between ultimate tensile strength (UTS) and YS (UTS−YS: 135 MPa). Such

---

* Corresponding author.
 E-mail address: zhangjinghuai@hrbeu.edu.cn (J. Zhang).

combination of high elongation and large UTS−YS value is difficult for most Mg alloys, including AZ31 alloy. In general, the elongation and UTS−YS value of AZ31 alloys are approximately 10–20% and 30–90 MPa, except for a few cases of AZ31 alloys prepared by special processes [12,13].

In this work, we reported a Mg-3Al-1Zn-0.4Mn (wt%) alloy (marked as H-AZ31 alloy) with high elongation (22%) and work-hardening capacity (UTS−YS: 164 MPa). Through the microstructure evolution analysis, we confirmed that introducing the heterogeneous grains in a certain size range is the main reason for the high formability potential of this AZ31 alloy.

The H-AZ31 alloy was prepared by the two-step extrusion: the as-cast commercial AZ31 alloy (diameter: 380 mm) was extruded at 275 °C with an extrusion ratio of 20:1 and a die-exit speed of 1.2 m min^{-1} in the first step, and then the one-step extruded alloy bar was extruded with an extrusion ratio of 25:1 and a die-exit speed of 2 m min^{-1} at 200 °C in the second step, and the finial diameter of extrusion bar is 15.5 mm (see Table S1 for details). The flat dog-bone tensile samples with gage length of 10 mm, width of 2 mm and thickness of 1 mm were cut by spark machining, mechanically ground, and electropolished by 10% perchloric acid alcohol solution at 20 V for 100 s at −20 °C. The tensile direction was parallel to the extrusion direction (ED), and the test was conducted at an initial strain rate with 1×10^{-3} s^{-1}. The scanning electron microscope (SEM, Quanta 250F) equipped with NordlysMax3 electron backscattered diffraction (EBSD) system was used to obtain EBSD data and secondary electron images with strains of 0%, 3%, 10%, and 17%. The EBSD results were dealt with the orientation imaging microscopy software Azteccrystal 2.1, and the slip trace analysis was calculated by the MATLAB code. Quantitative measures of surface displacements on tensile specimens with different strains were obtained using the atomic force microscope (AFM, Dimension Icon, Bruker). The dislocation structure was characterized by the transmission electron microscope (TEM, Talos F200X, Thermo Fisher Scientific, USA), and the thin-foil samples of TEM were prepared by ion-milling using PIPS II system (Gatan 695, USA) at −30 °C.

Fig. 1(a) shows the stress-strain curve of the H-AZ31 alloy. The YS of this alloy is approximately 113 MPa, while the UTS is as high as 277 MPa, showing a huge UTS−YS value of 164 MPa. Here, the UTS−YS value is used as a measure to evaluate the work-hardening capacity [10, 11]. Moreover, the alloy simultaneously displays a high elongation of failure, about 22%. As shown in Fig. 1(b), the H-AZ31 Mg alloy presents a superior combination of UTS−YS and elongation as compared to most reported wrought Mg alloys containing other AZ31 alloys [6–22], suggesting the higher formability of the H-AZ31 alloy.

The polycrystalline structure of the H-AZ31 alloy is illustrated in Fig. 1(c) by means of EBSD inversed pole figure (IPF) map referring to ED. The H-AZ31 alloy is completely recrystallized, and the average grain size is measured to be 8.2 μm (Fig. 1c). Fig. 1(d) presents the (0002) pole figures. The alloy shows a moderately strong basal texture (maximum intensity: 7.7), and large and small grains have similar texture intensity. It is worth noting that, unlike most fully recrystallized Mg alloys with roughly the same grain size [13], the grain size of H-AZ31 alloy in this study varies greatly, forming a typical heterostructure with multiple "small" grains surrounding "large" grains.

To better reveal the underlying deformation mechanism of this heterogeneous-grained structure, the grains are divided into two categories according to the grain size: "small" grains with size ≤ 10 μm and "large" ones with size ≥ 20 μm based on the statistical results of area-weight fraction vs. grain size, and the grains are also divided into three categories referring to the angle of deviation from normal direction (ND), i.e., 0–30° (texture components (TC) A), 30–60° (TCB), and 60–90° (TCC) tilting away from ND, referring to [23]. Based on the two classification standards (grain size and orientation), a total of 6 typical grains are selected for systematic analysis, i.e., grain A (TCA, "large"),
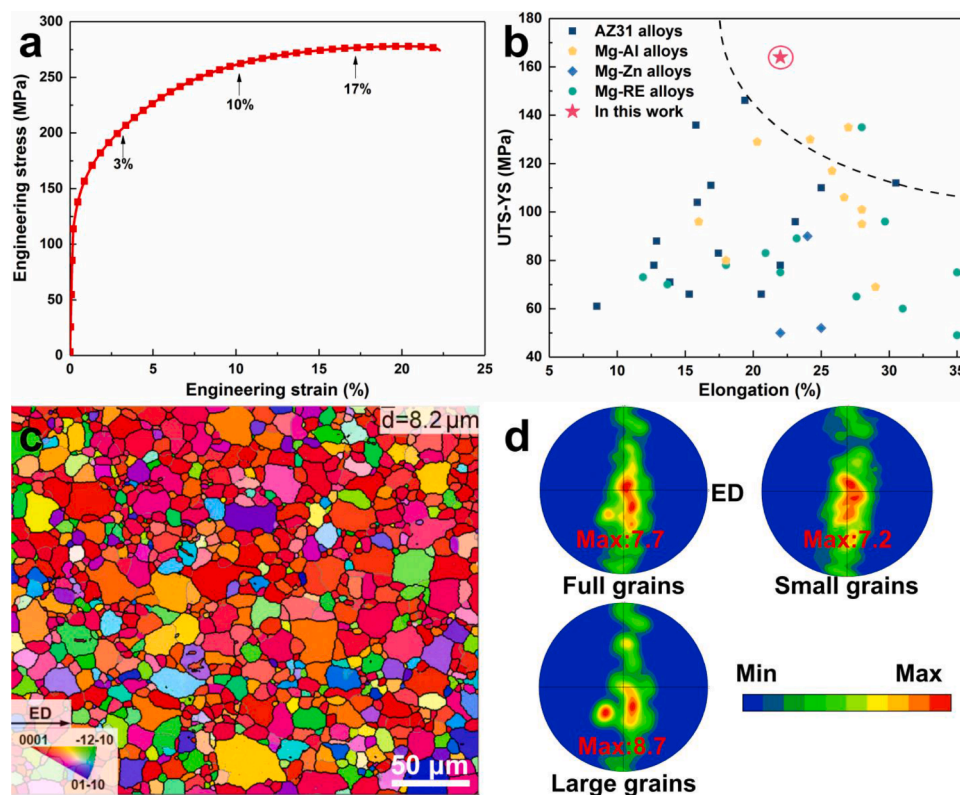

Fig. 1. (a) Tensile engineering stress-strain curve of H-AZ31 alloy; (b) distribution map of UTS−YS and elongation of the H-AZ31 alloy and other wrought Mg alloys (note that all data have been transformed into engineering stress and strain) [6–22]; (c) IPF map and (d) (0002) pole figures of full grains, small grains (≤ 10 μm), and large grains (≥ 20 μm) of the H-AZ31 alloy.

grain B (TCA, "small"), grain C (TCB, "large"), grain D (TCB, "small"), grain E (TCC, "large"), and grain F (TCC, "small"). Microstrains of typical grains under different engineering strains (0%, 3%, 10%, 17%) along the ED are analyzed based on the in-situ EBSD observation (Figs. 1c, 2, S1, and S2). In the initial stage of deformation (engineering strain up to 10%), the measured microstrains of "large" grain A, grain C, and grain E are only 1.3%, 0.9%, and 1.4%, while those of "small" grain B, grain D, and grain F are as high as 6.5, 6.1, and 8.6%, respectively. As for the later stage of deformation (engineering strain from 10% to 17%), the increased microstrains of all grains are roughly the same, about 4-5%. In addition, it is noted that there is no significant difference in microstrains between grains with similar sizes in different orientations.

In order to further explore the uneven deformation of "large" and "small" grains, the in-situ EBSD results were analyzed in detail. The deformation twinning rarely appear in the tensile deformation process, and thus almost all grains are deformed by dislocation slip (Figs. S1 and S2). As for slip trace analysis, all possible slip plane traces were calculated based on the average grain orientation information of the grain, and the slip system 11 (pyramidal I $\langle a \rangle$ slip $(-1101)[-1-120]$) is determined as the activated slip system (Fig. S3). Based on this method, all grains in Figs. 1(c) and S2 are analyzed, except a few grains that are too small to be analyzed, and the fraction of activated slip systems under different strains are calculated. The statistical results of activated slip

systems show that although the basal $\langle a \rangle$ dislocation slip is the dominant deformation mechanism, especially in the initial stage, the fraction of non-basal dislocation slips (including prismatic $\langle a \rangle$, pyramidal I $\langle a \rangle$ and II $\langle c + a \rangle$) increases significantly with the increase of strain. As for grain rotation, we define the angle between c-axis and tensile direction as θ_c, and the value of grain rotation (θ_{rot}) as the θ_c difference between two different strains. Based on the statistical results of Fig. 3(b), it is not difficult to find that the small grains tend to have an obviously higher θ_{rot}. The tensile strain rate jump test and AFM observation were used to analyze GB sliding during plastic deformation (see Supplementary Material for detailed process), and the results suggest that the contribution of GB sliding in this H-AZ31 alloy is quite limited (Fig. 4 and Table S2) [24,25].

The loading-unloading-reloading (LUR) stress-strain curve and back stress of the H-AZ31 alloy are illustrated in Fig. 3(c). The back stress (σ_b) can be calculated by the following equation [26–29]:

$$\sigma_b = \frac{(\sigma_u + \sigma_r)}{2} \tag{1}$$

where the σ_u and σ_r denote the unloading YS and reloading YS, respectively. It can be seen from Fig. 3(c) that the back stress of H-AZ31 alloy continuously reinforces with increasing tensile strains, which contributed to the high strain hardening. Fig. 3(d) shows the Kernel average
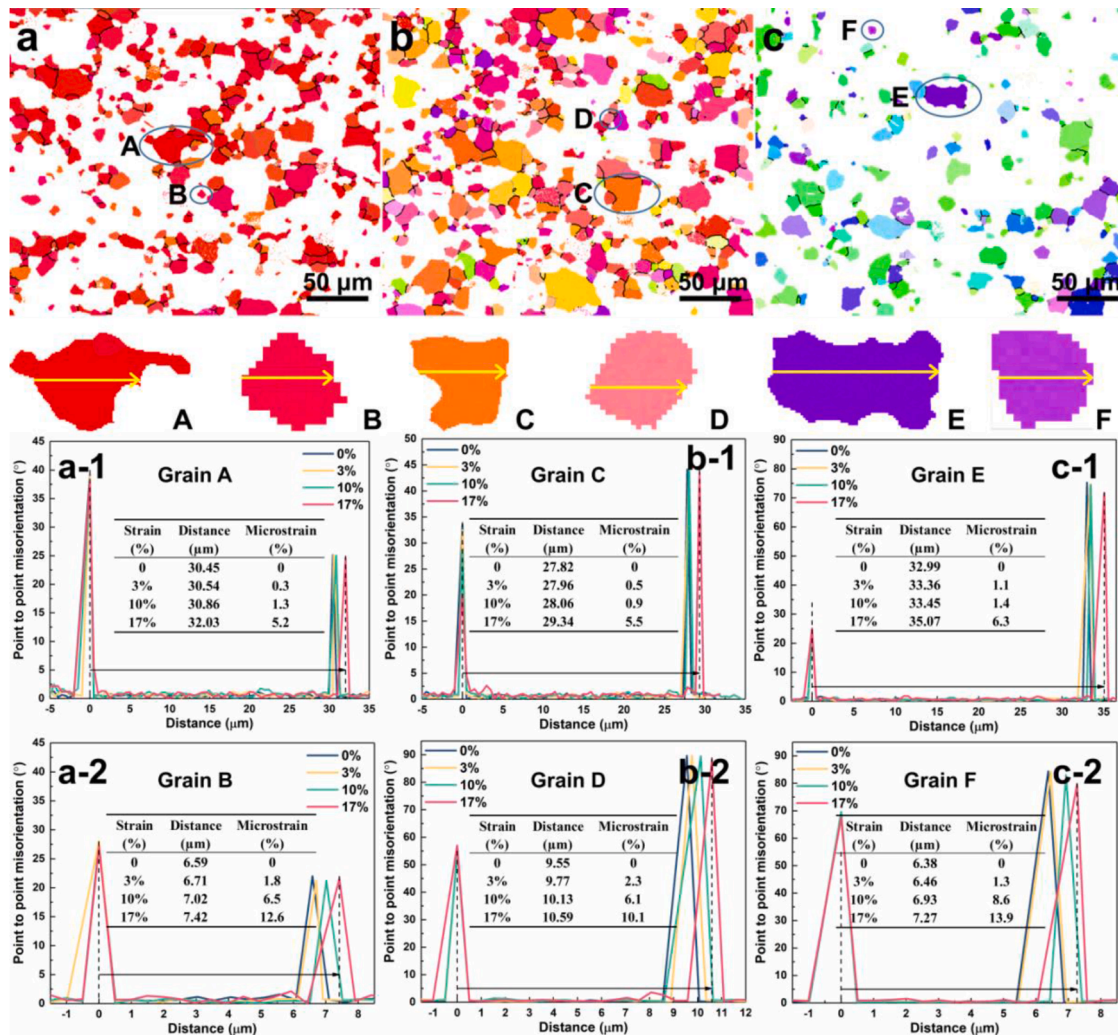

Fig. 2. Texture components maps of (a) TCA, (b) TCB, and (c) TCC groups; point to point misorientation measured along tensile direction (yellow arrow) with four strains (0%, 3%, 10%, 17%) of (a-1) grain A, (a-2) grain B, (b-1) grain C, (b-2) grain D, (c-1) grain E, and (c-2) grain F; "large" grain A and "small" grain B correspond to the position of the blue circles in (a), "large" grain C and "small" grain D correspond to the position of the blue circles in (b), "large" grain E and "small" grain F correspond to the position of the blue circles in (c).
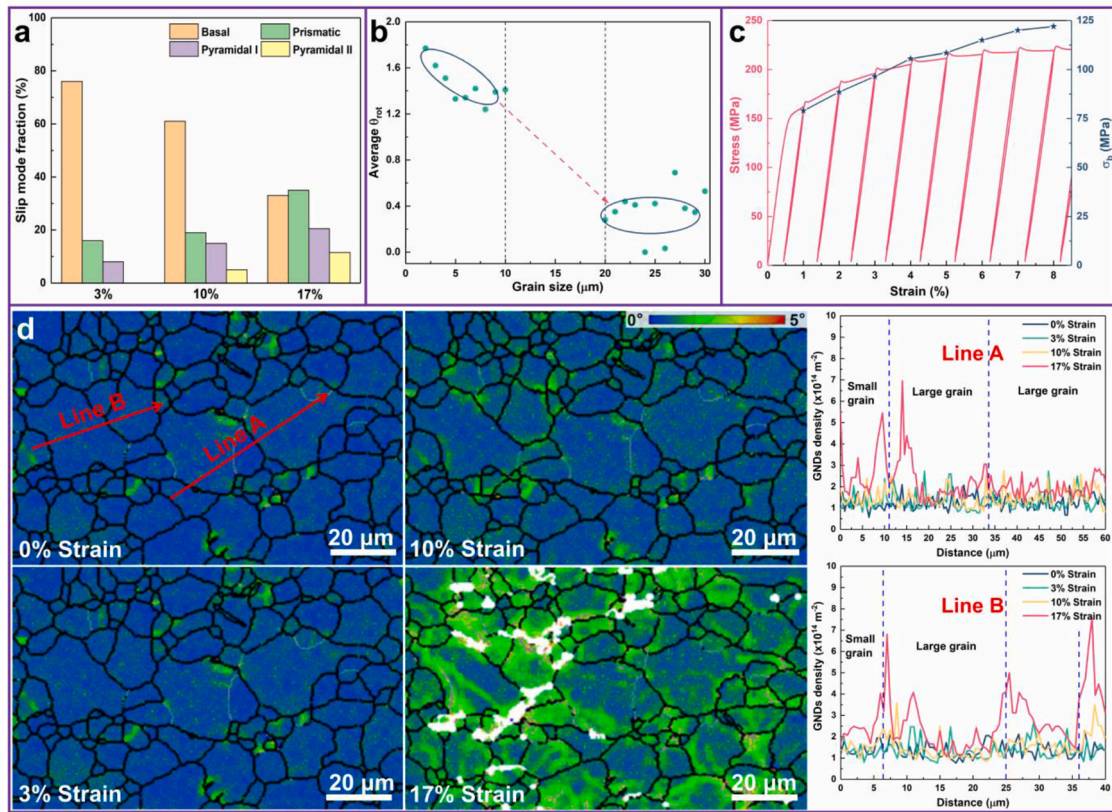
Fig. 3. (a) Statistics of the identified slip activity for H-AZ31 alloy under different strains. (b) Distribution of average θ_{rot} from 3% strain to 10% strain with respect to the grain size measured for the grains in Fig. 1(c). (c) LUR stress-strain curve and back stress. (d) KAM maps of typical location in Fig. 1(c) with different strains and corresponding GNDs density analysis at GBs.
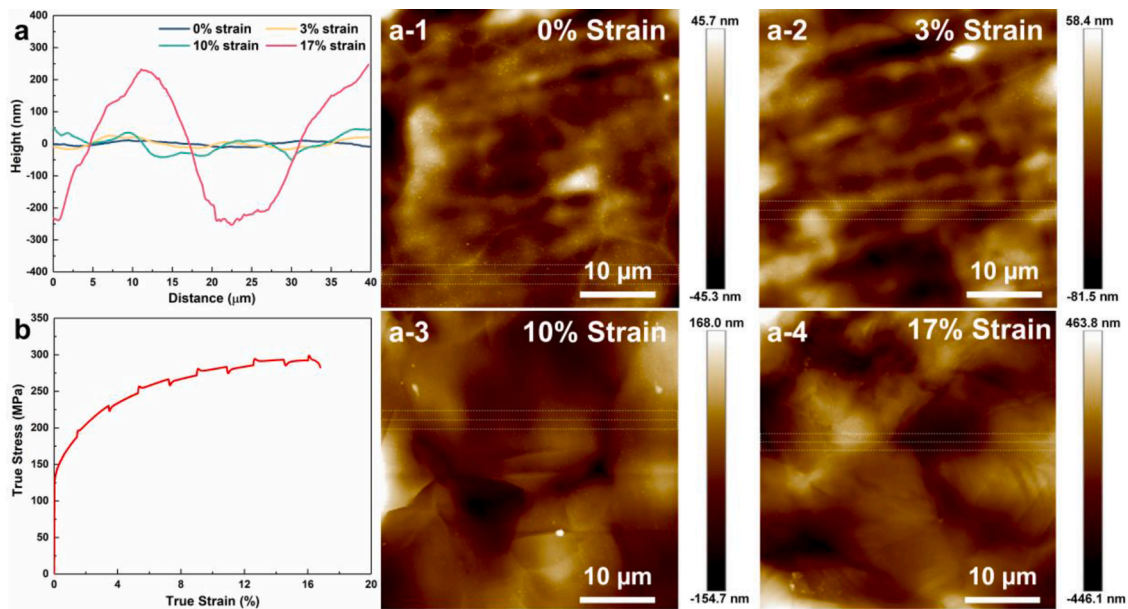

Fig. 4. GB sliding analysis of H-AZ31 alloy: (a) AFM image and height line profiles with different strains, (b) true stress-true strain curve obtained by the strain rate jump test.

miscorientation (KAM) maps of typical location in Fig. 1(c) under different strains. The geometrically necessary dislocations (GNDs) density (ρ_{GND}) can be calculated by the following equation [30]:

$$\rho_{GND} = \frac{2\overline{KAM}}{ub} \quad (2)$$

where u is equal to the scanning step length, and b is the Burgers vector of the gliding dislocations (~0.23 nm for Mg alloys). Upon plastic deformation, the GNDs density at the GBs between large and small grains increases significantly. The increased GNDs density at these GBs corresponds to the increase of back stress.

Fig. 5 shows the bright field (BF) and weak beam dark field (WBDF) TEM images with diffraction vector g = [0002] and [2–1–10] (or [01–10]) near the [01–10] (or [2–1–10]) zone axis in the typical grains of the H-AZ31 Mg alloy under 10% strain. Based on the invisibility criterion of defects, if the $g \cdot b$ = 0, the dislocations would be "out of contrast" (i.e., invisible). Basal ⟨a⟩ dislocations are dominant in both "small" and "large" grains, and there are also considerable pile-up non-basal dislocations around GBs.

In this work, the H-AZ31 Mg alloy with heterogeneous grains exhibits relatively low YS (113 MPa), large work-hardening capacity (UTS−YS: 164 MPa), and high elongation (~22%). The average grain size of the H-AZ31 alloy is about 8.2 μm, and the Hall-Petch slope (k value) and intercept (σ_0) of AZ31 alloys (basal texture; grain size > 2 μm) are about 205±10.6 MPa μm$^{1/2}$ and 124±4.5 MPa, respectively [31,32]. The YS of the H-AZ31 predicted by the Hall-Petch relationship is about 194 MPa, which is much higher than the YS obtained by experiment. Berbenni et al. [33] have reported that not only the average grain size plays a role but also the grain size distribution has an impact on the overall YS especially for fine-grained materials. In this work, the breakdown of the Hall-Petch relationship may be related to the internal stress and elastic stored energy between heterogeneous grains in the H-AZ31 alloy. In addition, the low-density pre-existing dislocations in the H-AZ31 alloy may also be one of the reasons for the low YS.

The H-AZ31 alloy in this work has moderately strong basal texture (Fig. 1d), relatively higher than other highly deformable Mg alloys [4,8,10], suggesting that the texture factor is not the main reason for good formability. There is almost no difference in texture intensity between small grains and large grains (Fig. 1d), indicating a different deformation mechanism with the reported bimodal microstructure [34–36]. The uneven deformation of such heterogeneous-grained structure is considered to be the critical reason for improving work-hardening capacity and ductility in this study. According to the results of microstrain calculation, the microstrain of "small" grains is dominant during the deformation process (Fig. 2). Based on the statistical results in Fig. 3(b), the average θ_{rot} values of "small" grains is significantly higher than "large" grains, indicating that the different grain rotation degree is at least one of the reasons for the uneven microstrains between "small" and "large" grains. The uneven deformation of heterogeneous grains of the H-AZ31 alloy leads to the strain gradient near GBs between "small" and "large" grains, which is surely different from the deformation state of uniform-grained Mg alloys. GNDs would be generated to accommodate the strain gradient, and the pile-up of GNDs impose the long-range back stress near these GBs, contributing to the high work-hardening capacity (Fig. 3c and d) [26].

The significant increase of non-basal dislocations (including prismatic ⟨a⟩, and pyramidal I ⟨a⟩ and II ⟨c + a⟩) during tensile deformation process is conducive to high ductility. The increase of non-basal slips of H-AZ31 alloy is obviously higher than that of most reported wrought Mg alloys with uniform grains [10], suggesting that the heterogeneous-grained structure promotes the activation of non-basal slips. Firstly, based on in-situ TEM observation, Liu et al. [37] have reported that the increased ⟨c + a⟩ dislocations slip may improve the ductility of Mg alloys at RT. Secondly, Zhao et al. [12] and Mayama et al. [38] found that the profuse prismatic ⟨a⟩ dislocation activities (Fig. 3a) would suppress twinning formation by rotating grains to preferred orientations for further deformation, leading a improved ductility. In this study, a considerable proportion of prismatic ⟨a⟩ dislocations are found (Fig. 3a) but there is almost no twinning even in large grains (Fig. S1) during deformation of the H-AZ31 alloy with large elongation, which is consistent with the previous results.

In summary, the H-AZ31 Mg alloy with high work-hardening capacity (UTS−YS: 164 MPa) and high elongation (~22%) has been prepared, which shows the potential for higher formability than other AZ31 alloys. The grain size difference rather than texture causes the uneven microstrain during plastic deformation. The pile-up of GNDs at GBs between large and small grains is responsible for the high work hardening. The significant increase of non-basal dislocations during deformation process induced by heterogeneous grains contributes to the improvement of ductility. Unfortunately, the YS of H-AZ31 alloy is rather low. Introducing similar heterogeneous structure to the high-strength Mg alloys may be expected to develop more ideal high-performance Mg alloys with good formability.
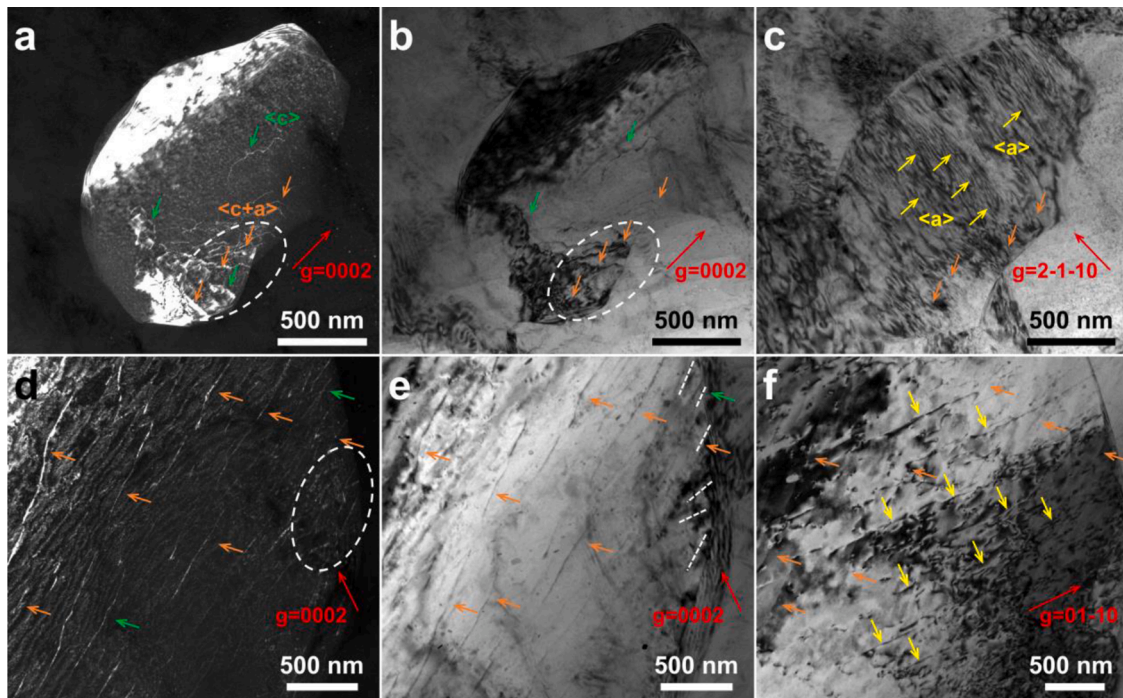

Fig. 5. BF and WBDF micrographs (using g = [0002] and g = [2–1–10] or [01–10]) revealing the ⟨c⟩ (green arrow), ⟨a⟩ (yellow arrow), and ⟨c + a⟩ (brown arrow) dislocations of (a-c) typical "small" grain ([01–10] zone axis) and (d-f) typical "large" grain ([2–1–10] zone axis) in the H-AZ31 alloy at 10% strain under ED tensile. White circles and short lines mark some pile-up non-basal dislocations at GBs.

Declaration of Competing Interest

The authors declare that they have no known competing financial interests or personal relationships that could have appeared to influence the work reported in this paper.

Acknowledgments

Supplementary materials

Supplementary material associated with this article can be found, in the online version, at doi:10.1016/j.scriptamat.2022.114963.

References

[1] B.C. Suh, M.S. Shim, K.S. Shin, N.J. Kim, Scr. Mater. 84-85 (2014) 1–6.
[2] J.S. Xie, J.H. Zhang, Z.H. You, S.J. Liu, K. Guan, R.Z. Wu, J. Wang, J. Feng, J. Magnes. Alloy. 9 (2021) 41–56.
[3] W.J. Joost, P.E. Krajewski, Scr. Mater. 128 (2017) 107–112.
[4] T.T.T. Trang, J.H. Zhang, J.H. Kim, A. Zargaran, J.H. Hwang, B.C. Suh, N.J. Kim, Nat. Commun. 9 (2018) 2522.
[5] Z. Zhang, J.H. Zhang, J.S. Xie, S.J. Liu, Y.Y. He, K. Guan, R.Z. Wu, Scr. Mater. 209 (2022), 114414.
[6] H. Zhang, G.S. Huang, L.F. Wang, J.H. Li, Scr. Mater. 67 (2012) 495–498.
[7] X.S. Huang, K. Suzuki, Y. Chino, Scr. Mater. 63 (2010) 395–398.
[8] X.S. Huang, M.Z. Bian, Y. Chino, Scr. Mater. 215 (2022), 114709.
[9] M.Z. Bian, X.S. Huang, Y. Chino, Acta Mater. 220 (2021), 117328.
[10] G.M. Zhu, L.Y. Wang, J. Wang, J. Wang, J.S. Park, X.Q. Zeng, Acta Mater. 200 (2020) 236–245.
[11] D.H. Kang, D.W. Kim, S. Kim, G.T. Ba, K.H. Kim, N.J. Kim, Scr. Mater. 61 (2009) 768–771.
[12] D.X. Zhao, X.L. Ma, A. Srivastava, G. Turner, I. Karaman, K.Y. Xie, Acta Mater. 207 (2021), 116691.
[13] Z.R. Zeng, Y.M. Zhu, R.L. Liu, S.W. Xu, C.H.J. Davies, J.F. Nie, N. Birbilis, Acta Mater. 160 (2018) 97–108.
[14] Z. Zhang, J.H. Zhang, J.S. Xie, S.J. Liu, Y.Y. He, R. Wang, D.Q. Fang, W. Fu, Y. L. Jiao, R.Z. Wu, Mater. Sci. Eng. A 831 (2022), 142259.
[15] Z.X. Wu, R. Ahmad, B.L. Yin, S. Sandlöbes, W.A. Curtin, Science 359 (2018) 447–452.
[16] X. Luo, Z.Q. Feng, T.B. Yu, J.Q. Luo, T.L. Huang, G.L. Wu, N. Hansen, X.X. Huang, Acta Mater. 183 (2020) 398–407.
[17] H. Somekawa, D.A. Basha, A. Singh, Materialia 8 (2019), 100466.
[18] H.Y. Wang, E.S. Xue, X.L. Nan, T. Yue, Y.P. Wang, Q.C. Jiang, Scr. Mater. 68 (2013) 229–232.
[19] P. Hidalgo-Manrique, J.D. Robson, M.T. Pérez-Prado, Acta Mater. 124 (2017) 456–467.
[20] C.J. Yan, Y.C. Xin, X.B. Chen, D.K. Xu, P. Chu, C.Q. Liu, B. Guan, X.X. Huang, Q. Liu, Nat. Commun. 12 (2021) 4616.
[21] T. Nakata, C. Xu, R. Ajima, K. Shimizu, S. Hanaki, T.T. Sasaki, L. Ma, K. Hono, S. Kamado, Acta Mater. 130 (2017) 261–270.
[22] T. Nakata, C. Xu, H. Ohashi, Y. Yoshida, K. Yoshida, S. Kamado, Scr. Mater. 180 (2020) 16–22.
[23] D.K. Guan, W.M. Rainforth, J.S. Gao, J. Sharp, B. Wynne, L. Ma, Acta Mater. 135 (2017) 14–24.
[24] R.X. Zheng, J.P. Du, S. Gao, H. Somekawa, S. Ogata, N. Tsuji, Acta Mater. 198 (2020) 35–46.
[25] C.F. Du, Y.P. Gao, Z.M. Hua, M. Zha, C. Wang, H.Y. Wang, Int. J. Plast. 154 (2022), 103300.
[26] X.L. Wu, M.X. Yang, Yuan F.P., G.L. Wu, Y.J. Wei, X.X. Huang, Y.T. Zhu, Proc. Natl. Acad. Sci. U. S. A. 112 (47) (2015) 14501–14505.
[27] Y. Wang, M. Chen, F. Zhou, E. Ma, Nature 419 (2002) 912–915.
[28] Y. Zhu, X. Wu, Mater. Res. Lett. 7 (2019) 393–398.
[29] S.S. Liu, D.B. Xia, H. Yang, G.S. Huang, F.X. Yang, X.H. Chen, A.T. Tang, B. Jiang, F.S. Pan, Int. J. Plast. (2022), https://doi.org/10.1016/j.ijplas.2022.103371.
[30] L.P. Kubin, A. Mortensen, Scr. Mater. 48 (2) (2003) 119–125.
[31] S.M. Razavi, D.C. Foley, I. Karaman, K.T. Hartwig, O. Duygulu, L.J. Kecskes, S. N. Mathaudhu, V.H. Hammond, Scr. Mater. 67 (5) (2012) 439–442.
[32] Z. Zhang, J.H. Zhang, J. Wang, Z.H. Li, J.S. Xie, S.J. Liu, K. Guan, R.Z. Wu, Int. J. Miner. Metall. Mater. 28 (2021) 30–45.
[33] S. Berbenni, V. Favier, M. Berveiller, Int. J. Plast. 23 (2007) 114–142.
[34] H. Zhang, H.Y. Wang, J.G. Wang, J. Rong, M. Zha, C. Wang, P.K. Ma, Q.C. Jiang, J. Alloy. Compd. 780 (2019) 312–317.
[35] Z.Z. Jin, M. Zha, Z.Y. Yu, P.K. Ma, Y.K. Li, J.M. Liu, H.L. Jia, H.Y. Wang, J. Alloy. Compd. 833 (2020) 155004.
[36] Z.Z. Jin, M. Zha, S.Q. Wang, S.C. Wang, C. Wang, H.L. Jia, H.Y. Wang, J. Magnes. Alloy. 10 (2022) 1191–1206.
[37] B.Y. Liu, F. Liu, N. Yang, X.B. Zhai, L. Zhang, Y. Yang, B. Li, J. Li, E. Ma, J.F. Nie, Z. W. Shan, Science 365 (2019) 73–75.
[38] T. Mayama, M. Noda, R. Chiba, M. Kuroda, Int. J. Plast. 27 (2011) 1916–1935.